CCFE
CULHAM CENTRE FOR FUSION ENERGY

UK Atomic Energy Authority

UKAEA-CCFE-PR(22)04

J. Peng, H Zhang, Y. Wang, M. Richardson, X. Liu, D. Knowles, M. Mostafavi

Correlation study on tensile properties of Cu, CuCrZr and W by small punch test and uniaxial tensile test

Correlation study on tensile properties of Cu, CuCrZr and W by small punch test and uniaxial tensile test

J. Peng, H Zhang, Y. Wang, M. Richardson, X. Liu, D. Knowles, M. Mostafavi

This is a preprint of a paper submitted for publication in Fusion Engineering and Design

Correlation Study on Tensile Properties of Cu, CuCrZr and W by Small Punch Test and Uniaxial Tensile Test

Jian Peng[1,2], Hao Zhang[1], Yiqiang Wang[2], Mark Richardson[2], Xuedong Liu[1], David Knowles[3], Mahmoud Mostafavi[3]

1 School of Mechanical Engineering, Changzhou University, Changzhou 213164 China

2 UKAEA, Culham Science Centre, Abingdon, Oxfordshire OX14 3DB, UK

3 Department of Mechanical Engineering, University of Bristol, Bristol BS8 1TR, UK

ABSTRACT: The small punch test (SPT) has been widely used to evaluate the mechanical properties of materials for the nuclear industry due to its advantage of requiring minimal sample volumes. In this paper, the correlation between SPT and uniaxial tensile testing (UTT) is investigated for three materials used in the plasma-facing components of fusion reactors, namely Cu, CuCrZr alloy and W, whose mechanical properties vary significantly. From the views of mechanical properties and fracture morphologies, materials demonstrate consistent behaviours between SPT and UTT, which proves that the SPT is an effective method to characterize the mechanical properties and fracture mechanism of Cu, CuCrZr alloy and W. Moreover, the finite element simulation results of SPT for five other copper alloys with different mechanical properties are added, and the quantitative correlation equations of mechanical properties between SPT and UTT are established. One unified correlation equation between SPT and UTT can be established for the ductile materials with largely different mechanical properties. However, the introduction of a brittle material in the form of W invalidated the correlation equation. This work provides a reference for the study of mechanical properties of materials used in plasma-facing components by SPT.

Keywords: Small punch test; Cu, CuCrZr, W; Tensile property; Correlation method

1 Introduction

The International Thermonuclear Experimental Reactor (ITER) project is an international scientific research cooperation project to study nuclear fusion energy, and the key research and development of materials for fusion applications have laid a strong technological foundation to support the energy landscape of fusion [1]. The divertor is a key component in ITER, the function of which is to discharge the energy, particle flow and helium ash produced by the fusion reaction [2]. Tungsten (W) is considered an ideal plasma-facing material for the divertor because of its good thermal conductivity, thermal shock resistance, high melting point and low retention of hydrogen isotopes [3]. CuCrZr alloy has high strength and thermal conductivity even at high temperature, and the material damage caused by irradiation can also be reduced by element doping of CuCrZr alloy, while Cu has excellent thermal conductivity. Therefore, Cu and CuCrZr alloys are usually used as heat sink materials in the divertor [3, 4]. The full-scale tubular W-Cu module developed by Japan [5] has passed the high heat load test

and meets the high heat load requirements of ITER, and Europe [6, 7] has carried out high heat load tests on small-scale through-tube W-Cu modules and full-size divertor target plate components and determined the critical heat load flux. Meanwhile the Experimental Advanced Superconducting Tokamak (EAST) developed by China [8, 9] adopted the W divertor and verified the high heat load performance of W-Cu modules. The study of the mechanical properties of Cu, CuCrZr and W plays an important role in ensuring the safety of plasma-facing components in thermonuclear fusion equipment [10].

The small punch test (SPT) is a test method for evaluating the mechanical properties of materials using small, disk-shaped specimens. Compared with the standard tensile method, the required sample volume is very small, and it is considered as a non-destructive (semi non-destructive) test for evaluating mechanical properties. SPT was primarily developed to study the irradiation damage on the mechanical properties of nuclear materials [11] and has been widely used in the nuclear industry. Mechanical properties including yield stress [12], tensile strength [13], ductile-brittle transition temperature [14], fracture toughness [15] and high temperature creep [16] have been successfully estimated for a wide range of materials. Based on a comparison of the effects from mechanical properties, damage parameters, friction coefficients, pre-tightening conditions and geometric uncertainty, the factors influencing SPT were ranked in order of sensitivity to improve understanding of this test method [17]. In-situ digital image correlation (DIC) technology was employed in SPT to estimate tensile properties with the advantage of deflection mapping [18]. In addition to experimental studies of SPT, researchers used finite element simulation and neural network methods combined with SPT to determine the tensile mechanical properties [19].

SPT is widely used in the study of mechanical properties for nuclear materials. Kumar et al. [20] used SPT data to determine GTN model parameters for the structural materials of nuclear reactors, and proved the feasibility of using SPT to determine the J-R data of irradiated materials by comparing finite element simulation results with actual test results. Simonovski et al. [21] calibrated the fitting coefficients in the correlation equation between tensile strength and the maximum load of SPT with the flat SPT specimen, indicating that the same correlation equation can be used to estimate the tensile strength of fuel cladding tubes at 650 °C. Simonovski et al. [22] applied the GTN model in the finite element simulation of SPT to evaluate the crack initiation and propagation, and found that the damage parameters significantly influenced the maximum force of the load-displacement curve. Zhang et al. [23] used SPT combined with finite element simulation and a sequential programming algorithm to characterize the constitutive relationship of high-energy heavy-ion irradiated steel. The resulting constitutive relationship was found to be consistent with the experimental load-displacement curve of the irradiated sample. Yao et al. [24] used the SPT to determine the ductile-brittle transition temperature (DBTT) for the materials Optifer-IX, Eurofer 97 and MA956 steels after irradiation, and

found that the DBTT of the three steels increased with irradiation dose, which agreed well with Charpy impact tests. SPT was used to understand the variation in mechanical properties and damage parameters for quenched and aged CuCrZr used in plasma-facing components [25]. The creep behaviour of Eurofer97 and 14Cr Oxide Dispersion strengthened steel were assessed via SPT by Richardson et al. [26], and the applicability of the equivalent uniaxial creep stress method was discussed for two materials.

The mechanical properties of Cu, CuCrZr and W vary considerably, and therefore provide an ideal basis for study via SPT. In this paper, SPT, uniaxial tensile test (UTT), finite element simulation, and fracture analysis are carried out on Cu, CuCrZr and W, and the correlation equations between SPT and UTT for these materials are constructed. The research results of SPT on Cu, CuCrZr and W are thus helpful in evaluating the mechanical properties of materials used in plasma-facing components.

2 Materials, experimental and simulation methods

2.1 Cu, CuCrZr and W

Cu, CuCrZr and W are typical materials used in plasma-facing components. Cu has good plastic deformation behaviour and can withstand cold and hot plastic processing, but its strength is low. CuCrZr has relatively high strength and toughness at high temperature. Although W has high hardness and high melting temperature, it also exhibits a ductile to brittle transition, leading to a pronounced brittleness at low temperature. The materials used in this study (Cu, CuCrZr and W) were provided by Guantai Metal Material Co., LTD (Hebei province, China) in plate form with a thickness of 14mm. The chemical compositions are listed in Table 1.

Table 1 Chemical compositions of Cu, CuCrZr, W (all in weight %)

	Cu	Sb	As	Fe	Pb	S	Cr	Zr	W	Si	Mo	Ni	P
Cu	Bal.	0.002	0.001	0.003	0.002	0.002	—	—	—	—	—	—	—
CuCrZr	Bal.	—	—	—	—	—	0.73	0.09	—	—	—	—	—
W	—	0.001	—	0.0005	—	—	—	—	Bal.	0.001	0.001	0.0005	0.001

2.2 SPT, UTT and fracture surface observation

The schematic diagram of the SPT device is shown in Fig. 1(a), which consists of an upper die, lower die, Φ 2.5 mm Si_3N_4 ceramic ball, and punch. The test specimen consists of a metal disk with a diameter of 10 mm and thickness of 0.5 mm, and sits between the upper and lower dies for clamping and fixing. The lower die has a receiving hole with a diameter of 4 mm and a chamfer by 0.2 mm(45°). The constant displacement loading rate of 0.1 mm/min is applied to the ball by the punch until the sample is fractured, while the punch load and punch displacement data are recorded to construct the SPT load-displacement curve. The structural dimensions of the SPT device and test

process meet the requirements of SPT standard GB/T 29459. 2-2012 [27], and three repeated tests are carried out for each material.

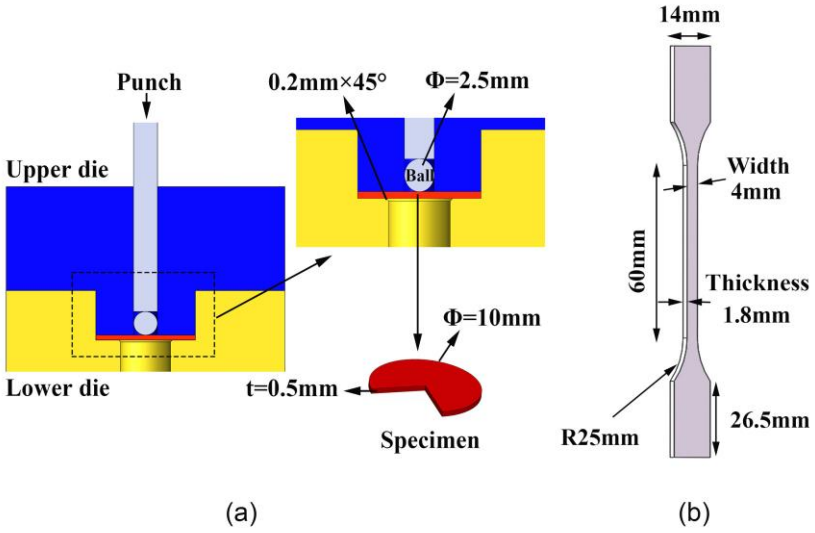

Fig. 1 Dimensions of specimens: (a) SPT specimen; (b) UTT specimen.

For comparison with the SPT results, UTT is carried out for all three materials. The specimen dimensions are given in Fig. 1(b). The sample length is parallel to the rolling direction of the metal plate, and testing processes meet the requirements of the UTT standard GB/T 228. 1-2010 [28]. The UTT was carried out by the 10t electronic universal mechanical testing machine (SUNS UTM5105). All tests were carried out at room temperature, and a displacement loading rate of 0.5 mm/min was applied until specimen fracture occurred.

To understand the correlation of facture mechanism between UTT and SPT, the fracture surfaces were examined via Scanning Electron Microscopy (SEM, JEM-2100) for both UTT and SPT tested specimens.

2.3 Finite element simulation of SPT

Since both the test setup and load conditions are axially symmetric, the test can be simulated through a 2D axisymmetric model, as shown in Fig. 2. The sample is placed between the upper and lower dies. The upper die, lower die and ball are modelled as analytical rigid bodies, while the sample is modelled as a deformable body. The load and boundary conditions used in the simulation agree with those in the test. All movements of upper and lower dies are fixed, while only the vertical movement of the punch ball is free and other directions are also fixed. The displacement load is applied on the punch ball and then transferred to the SPT sample. Surface-to-surface contact is defined between the sample and the upper and lower dies as well as between the sample and the punch ball. The penalty formula is used with a friction coefficient of 0.2. An eight node, bi-directional quadratic axisymmetric quadrilateral element with the reduced integral (CAX8R) is used

to mesh the sample. The mesh is refined at the contact surface between the punch and the sample with a mesh size of 0.01mm, while the mesh size gradually increases towards the edge of the sample. The model has 25333 nodes and 8300 elements, which are to balance the simulation accuracy and the simulation time.

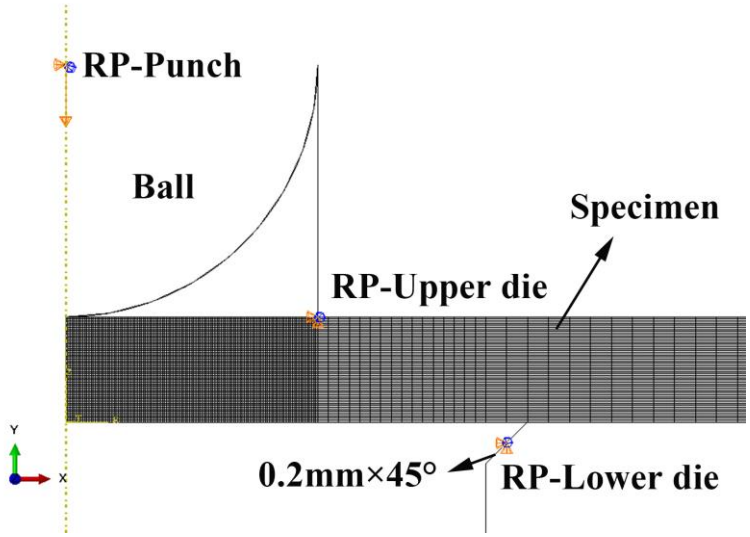

Fig. 2 Geometric model and mesh of SPT.

3 Results and Discussion

3.1 SPT results

The load-displacement curves of Cu, CuCrZr and W obtained by SPT are shown in Fig. 3. It can be seen that the repeatability of SPT for Cu and CuCrZr is good, and any divergence mainly appears at the failure stage. However, greater variability appears for W at the fracture stage, which may be related to the brittle nature of the material. The load-displacement curves of both Cu and CuCrZr contain five complete stages, which reflect the typical characteristics of a ductile material. It can also be seen that the yield load and maximum load of CuCrZr are significantly higher than those of Cu. However, the load-displacement curve of W only contains the elastic stage and fails at a very low displacement, indicating a brittle failure.

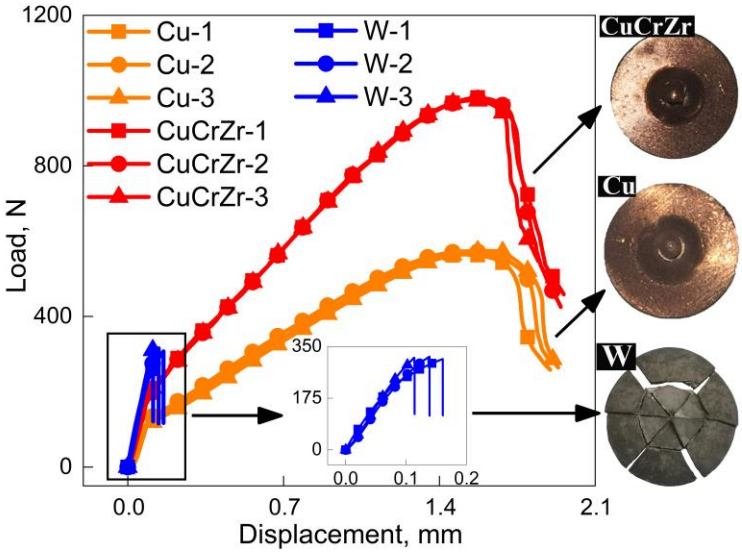

Fig. 3 Load-displacement curves and fracture modes of SPT for Cu, CuCrZr and W.

Based on the load-displacement curve in Fig. 3, the characteristic parameters of SPT can be obtained, including yield load, maximum load, displacement at maximum load, etc. Because the transition point from the elastic stage to plastic stage in SPT is not clearly defined, several determination methods have been proposed. The yield load P_{y_Mao} was defined by Mao and Takahashi [29] as the intersection point of two tangent lines of the elastic stage and the plastic stage. The tangent of the elastic stage corresponds to the maximum slope in the elastic region, while the tangent of the plastic region corresponds to the minimum slope in the plastic region. Another yield load determination method was the modified Mao method [30] named P_{y_CEN}, which was applied in the *CEN* SPT standard [31]. P_{y_CEN} is defined as the vertical projection of the intersection point of two tangent lines on the SPT curve. Moreover, the yield load $P_{y\_t/10}$ using a method similar to the yield stress $R_{p0.2}$ in the standard UTT was proposed [32], and the intersection point of the tangent line of the elastic region after translation *t/10* and the load-displacement curve is defined as $P_{y\_t/10}$. Fig. 4 gives the three yield load determination methods.

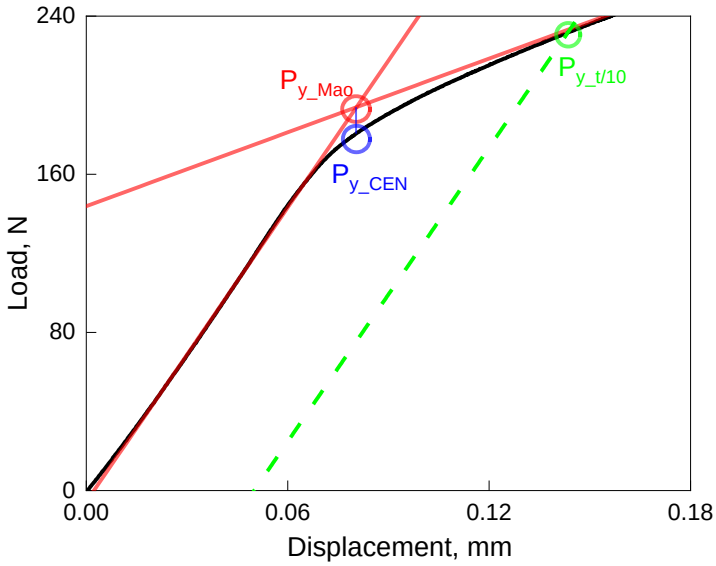

Fig. 4 Comparison of the determination methods for the yield load.

The yield loads, maximum loads (P_m) and displacements corresponding to maximum load (d_m) determined from the load-displacement curves of Cu, CuCrZr and W are listed in Table 2. This includes the use of all three yield load determination methods illustrated in Fig. 4. From the quantitative comparison of the mechanical parameters of SPT in Table 2, it can be found that the yield load and the maximum load of CuCrZr are significantly higher than those of Cu, but their fracture displacements are similar, while the fracture displacement of W is significantly smaller, being one order of magnitude less than those of Cu and CuCrZr, which reflects the typical brittleness.

Table 2 Mechanical parameters of SPT for Cu, CuCrZr, W

Material	t/mm	P_{y_Mao}/N	P_{y_CEN}/ N	$P_{y\_t/10}$/ N	P_m/ N	d_m/mm
Cu-1	0.500	113.7	109.3	128.6	565.0	1.520
Cu-2	0.501	131.2	125.2	137.6	573.3	1.518
Cu-3	0.499	106.6	103.0	122.6	574.2	1.619
Cu-Mean	**0.500**	**117.2**	**112.5**	**129.6**	**570.8**	**1.552**
CuCrZr-1	0.500	207.3	166.2	215.6	981.6	1.578
CuCrZr-2	0.499	203.2	188.6	230.0	979.9	1.568
CuCrZr-3	0.501	217.8	190.7	232.1	974.4	1.553
CuCrZr-Mean	**0.500**	**209.4**	**181.8**	**225.9**	**978.7**	**1.566**
W-1	0.500	—	—	—	307.4	0.160
W-2	0.500	—	—	—	315.3	0.138
W-3	0.498	—	—	—	312.1	0.113
W-Mean	**0.499**	**—**	**—**	**—**	**311.6**	**0.137**

3.2 UTT results

To compare with the results of SPT, the true stress-true strain curves of Cu, CuCrZr and W obtained by UTT are shown in Fig. 5. Yield stress, tensile strength, and fracture elongation are determined from the true stress-true strain curves of three materials, which are summarized in Table

3.

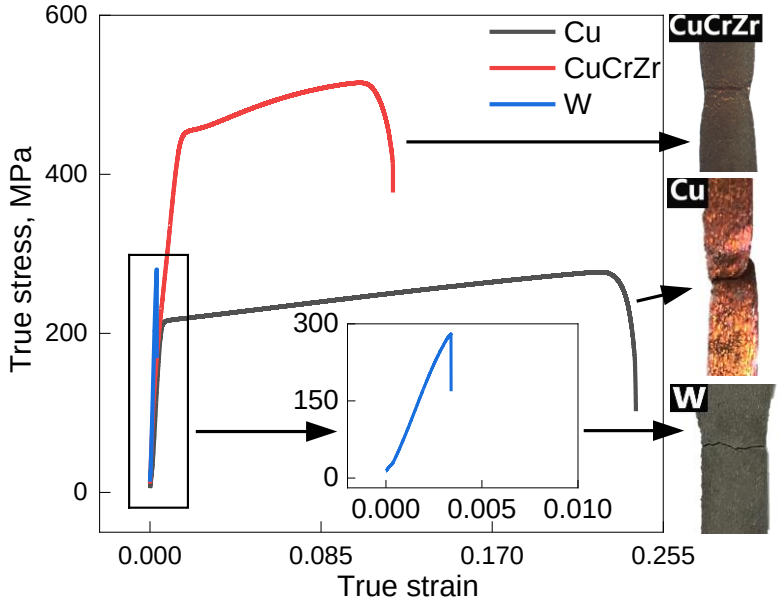

Fig. 5 True stress-true strain curves and fracture modes of UTT for Cu, CuCrZr, W.

Table 3 The mechanical properties of UTT for Cu, CuCrZr, W

Material	$R_{p0.2}$/MPa	R_m/MPa	A/%
Cu	211.87	223.34	27.45
CuCrZr	445.21	466.87	12.57
W	—	279.24	0.53

From both the qualitative curves in Fig. 5 and the mechanical properties in Table 3, it can be seen that Cu and CuCrZr are typical ductile materials with obvious plastic deformation and hardening behaviour, while W exhibits a typically brittle failure, having fractured at low strain and under elastic deformation. Because CuCrZr contains strengthening alloy elements, the yield stress and tensile strength of CuCrZr are significantly higher than those of Cu, but the fracture elongation of Cu is about twice that of CuCrZr.

From the qualitative comparison between the load-displacement curves of SPT in Fig. 3 and the true stress-true strain curves of UTT in Fig. 5, material behaviour is consistent across SPT load-displacement curves and UTT stress-strain curves, which proves that SPT can effectively characterize the toughness and brittleness for Cu, CuCrZr and W. However, it should be noted that from the quantitative comparison of the mechanical properties between SPT in Table 2 and UTT in Table 3, their variations with material are different, and correlation equations need to be established.

3.3 Finite element simulation results of SPT

Although Cu, CuCrZr and W cover ductile and brittle characteristics, three testing materials alone are insufficient to construct the qualitative correlation equations of the mechanical parameters between SPT and UTT. To understand the correlation between SPT and UTT, besides the

experimental data, finite element simulation results of SPT for five other copper alloys with different strengths and ductility in literatures [33, 34] are added to complement the data. The mechanical properties of copper alloys with different strengths and ductility are listed in Table 4, while the yield stress covers the range from 46.19 MPa to 410.92 MPa, the tensile strength covers the range from 215.81 MPa to 444.36 MPa, and the fracture elongation covers the range from 16% to 47%.

Table 4 Mechanical properties of copper alloys used in the simulation [33, 34]

Material	E/MPa	$R_{p0.2}$/ MPa	R_m/ MPa	A/%
C122AN	104110	46.19	215.81	45
C715	151680	128.93	398.51	47
C464	965270	213.74	436.44	37
C102	119280	322.67	333.71	17
C150	108940	410.92	444.36	16

To verify the reliability of the finite element simulation of SPT, uniaxial tension test data of Cu and CuCrZr are inputted in the finite element simulation of SPT, and the load-displacement curves obtained by simulations are compared with those obtained by SPT experiments for Cu and CuCrZr. As shown in Fig. 6, the load-displacement curves obtained by finite element simulation agree well with those of experiments, and the deviation only exists at the failure stage, which suggests that the finite element simulation method can effectively predict the load-displacement curve of SPT.

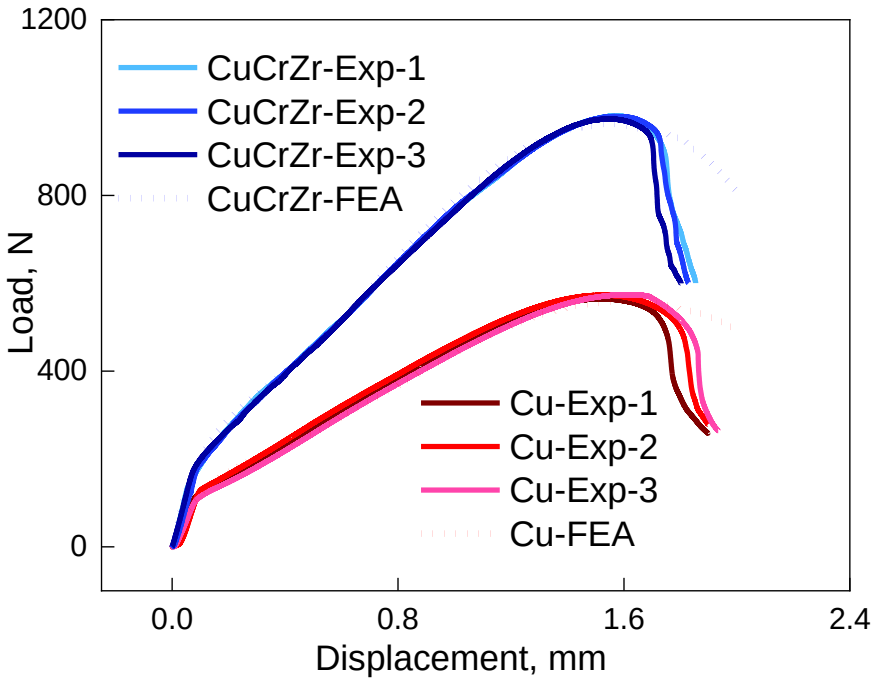

Fig. 6 Comparison of load-displacement curves between finite element simulation and experiment.

The load-displacement curves of five copper alloys obtained by finite element simulation are shown in Fig. 7. Then the yield load, the maximum load, and the displacement at maximum load are determined from the load-displacement curves, as listed in Table 5. Comparing the mechanical properties of SPT by simulation in Table 5 and the mechanical properties of UTT in Table 4, there

are positive correlations between SPT parameters and UTT parameters including: yield load vs. yield stress, the maximum load vs. tensile strength, and the displacement at maximum load vs. fracture elongation. Therefore, both the experimental SPT results of Cu, CuCrZr and W and the simulated results of five other copper alloys show that the mechanical parameters of SPT can be correlated with the mechanical properties of UTT.

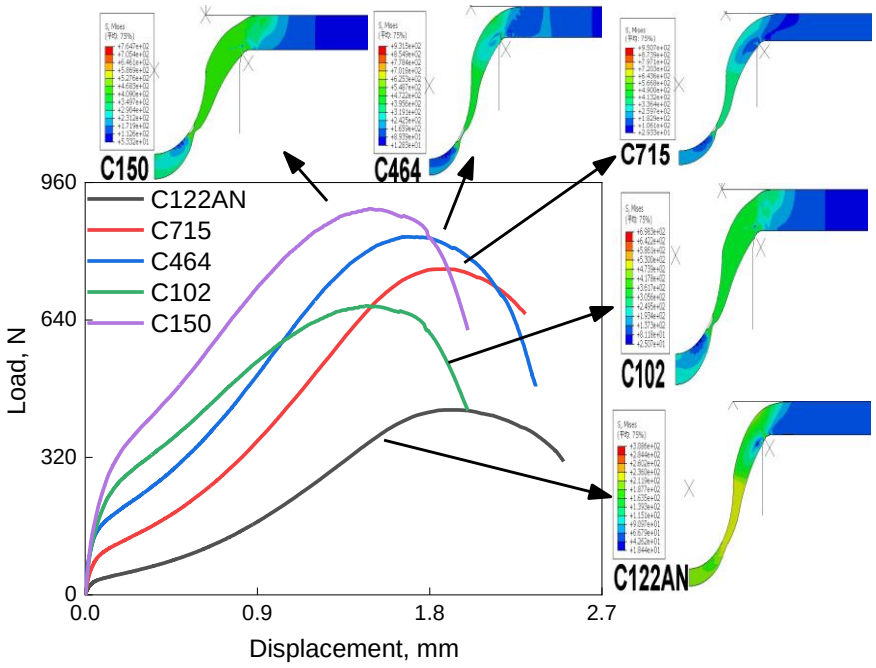

Fig. 7 Load-displacement curves obtained by finite element simulation.

Table 5 Mechanical parameters of SPT for five copper alloys by finite element simulation

Material	P_{y_Mao}/MPa	P_{y_CEN}/MPa	$P_{y\_t/10}$/MPa	P_m/MPa	d_m/mm
C122AN	32.54	26.21	40.06	430.66	1.94
C715	87.89	74.31	104.16	758.61	1.89
C464	152.21	133.78	176.87	833.62	1.69
C102	227.25	185.17	234.91	673.02	1.47
C150	278.61	226.32	303.53	898.87	1.48

3.4 Fracture mechanisms of SPT and UTT

To understand the correlation of fracture mechanisms between SPT and UTT, the fracture morphologies of both methods for Cu, CuCrZr and W were observed and compared via SEM as shown in Fig. 8.

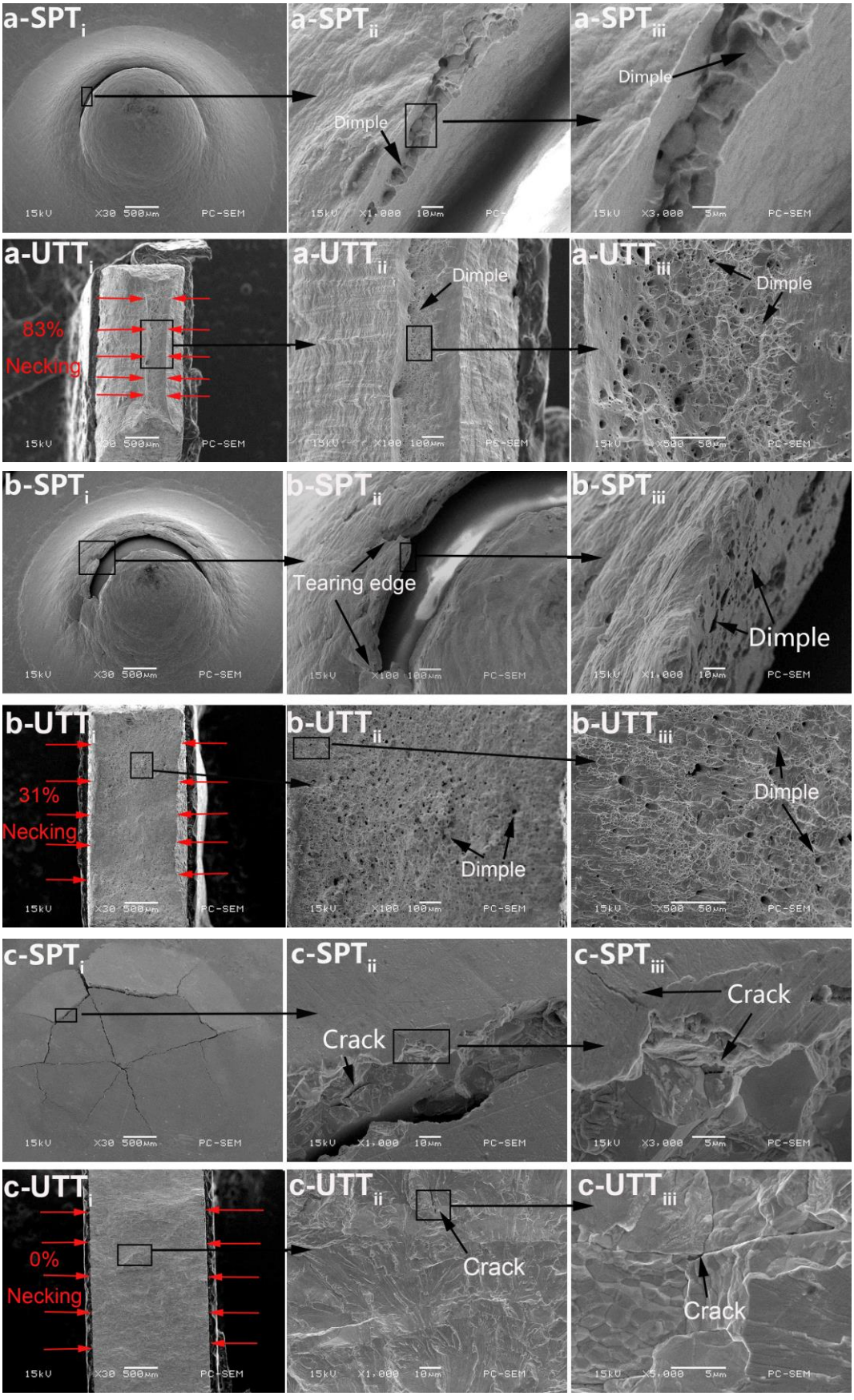

Fig. 8 Comparison of fracture morphologies between SPT and UTT: (a) Cu; (b) CuCrZr; (c) W.

From Fig. 8 (a-SPT), the SPT fracture sample of Cu shows the circumferential necking fracture

morphology without crack, while from Fig. 8 (a-UTT), the UTT fracture sample of Cu shows the very significant necking, with an 83% reduction of area at fracture. Based on the enlarged fracture morphologies of SPT and UTT for Cu in Fig. 8 (a-SPT) and Fig. 8 (a-UTT), there are many dimples of different sizes at the fracture surfaces of both tested samples. The dimple holes at the fracture edge are large and deep, and the dimples at the center are small and dense. Therefore, based on the comparison of fracture morphologies of SPT and UTT, both samples of Cu fractured by the ductile fracture mechanism with significant plastic deformation.

As shown in Fig. 8 (b-SPT), the SPT fracture sample of CuCrZr shows the mixed circumferential necking and a few radial tearing edges, while as shown in Fig. 8 (b-UTT), the UTT fracture sample of CuCrZr shows the necking phenomenon, but the reduction of area of CuCrZr is about 31%, significantly lower than that of Cu in Fig. 8 (a-UTT). According to the enlarged fracture morphologies of SPT and UTT of CuCrZr in Fig. 8 (b-SPT) and Fig. 8 (b-UTT), the dense and shallow dimples are uniformly distributed at the fracture surfaces of both SPT and UTT fractured samples, and the radial tearing edges of SPT are caused by the combination of large dimples. Therefore, based on the comparison of fracture morphologies of SPT in Fig. 8 (b-SPT) and UTT in Fig.8 (b-UTT), both samples of CuCrZr failed by a ductile fracture mechanism, though the deformability is less than that of Cu.

As shown in Fig. 8 (c-SPT), the SPT fracture sample of W shows a pure brittle fracture morphology with mixed circumferential and radial cracks, while in Fig. 8 (c-UTT), the UTT fracture sample of W shows the typical brittle character without any necking. According to the enlarged fracture morphologies of SPT and UTT of W in Fig. 8 (c-SPT) and Fig. 8 (c-UTT), brittle fracture of W is caused by intergranular fracture. Therefore, the fracture mechanism of W for both SPT and UTT are the same pure brittle fracture.

Fig. 8 shows that Cu, CuCrZr and W samples tested under SPT and UTT have similar fracture morphology characteristics. This highlights SPT as a promising method that can be adopted to understand the fracture mechanisms of Cu, CuCrZr and W.

3.5 Correlation of SPT and UTT

3.5.1 Correlation between yield load and yield stress

Mao and Takahashi [29] proposed a linear relationship between yield stress and yield load, and gave the correlation formula as Eq. (1):

$$R_{\mathrm{p0.2}} = \alpha_1 \cdot \frac{P_y}{t^2} + \alpha_2 \qquad (1)$$

where α_1 and α_2 are the correlation parameters, t is the sample thickness, $R_{P0.2}$ is the yield stress, and P_y is the yield load of SPT. Eq. (1) was applied to predict the yield stress from SPT yield load for steels in the NIST research report [35], in-service pipe steel [36], PM aluminium composites [37] and additively manufactured materials [38].

To understand the applicability of Eq. (1) to Cu and CuCrZr, Fig. 9 gives the relationship between yield load and yield stress, and P_{y_Mao}, P_{y_CEN}, and $P_{y\_t/10}$ are all considered to compare their differences. In Fig. 9, the points correspond to the experimental and simulated results, while the line is fitted according to Eq. (1). Since W was too brittle to exhibit a yield stress, only the experimental results of Cu and CuCrZr, and the simulated results of five other copper alloys are given. It can be seen that both the experimental data points and the simulated data points support the positive correlation between yield load and yield stress. Among P_{y_Mao}, P_{y_CEN}, and $P_{y\_t/10}$, the correlation coefficient corresponding to P_{y_CEN} in the *CEN* standard is the highest. Therefore, although the materials vary significantly in strength, a uniform correlation equation of yield load and yield stress can be established for the ductile materials.

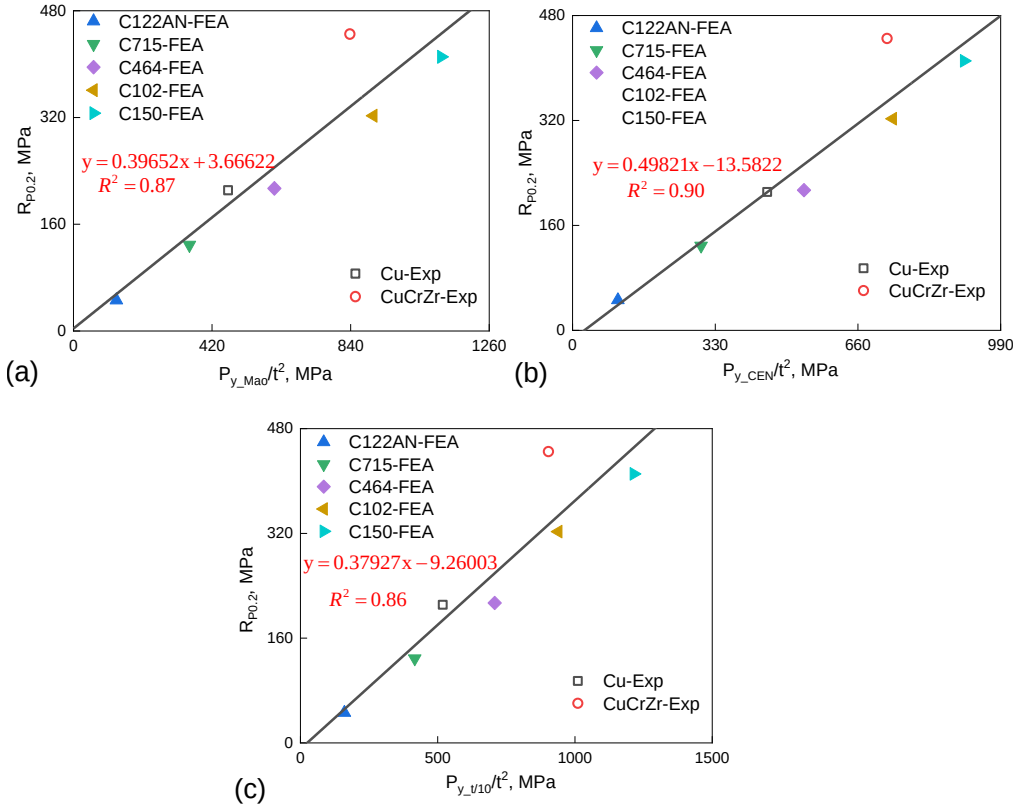

Fig. 9 Correlation between yield load and yield stress: (a) P_{y_Mao}; (b) P_{y_CEN}; (c) $P_{y\_t/10}$.

3.5.2 Correlation between the maximum load and tensile strength

Mao and Takahashi [29] proposed a correlation in the form of Eq. (2), between maximum load and tensile strength that incorporated the effect of sample thickness. To consider the influence of

displacement at maximum load, another correlation equation was proposed in the form of Eq. (3) [39].

$$R_m = \beta_1 \cdot \frac{P_m}{t^2} + \beta_2 \quad (2)$$

$$R_m = \beta_1' \cdot \frac{P_m}{t \cdot d_m} + \beta_2' \quad (3)$$

where β_1, β_2, β_1' and β_2' are correlation parameters, R_m is the tensile strength, P_m is the maximum load, d_m is the displacement at maximum load. Both correlation equations were applied and compared for the suitability of steels in the NIST Research Report [35]. Kumar et al. [40] used Eq. (2) to predict the tensile strengths of 20MnMoNi55, CrMoV steel and SS304LN. The application of Eqs. (2) and (3) were discussed for nine steel alloys by Chica et al. [41]. In addition to the steels, these correlation equations were applied to PM aluminum composites [37] and additively manufactured materials [38].

To understand the applicability of correlation equations of the maximum load and tensile strength to Cu, CuCrZr and W used in plasma-facing components, Figs. 10 (a) and (b) give the relationship between the maximum load and tensile strength based on Eqs. (2) and (3) respectively. The points correspond to the experimental and simulated results, while the lines are fitted according to the correlation equations. Since the mechanical behaviour of W is completely different to the ductile materials, two fitting lines are compared in Fig. 10, where the red solid lines named as “Fit with W” are fitted to the data of both ductile materials and brittle W, and the blue dashed lines named as “Fit without W” are fitted only to the data of ductile materials. With regard to the blue dashed line, although the ductile materials cover a wide strength range, one uniform equation can be observed, and Eq. (2) provides the higher correlation coefficient of 0.95. However, if the data of both ductile materials and brittle W are considered in the fitting, corresponding to the red solid line, both correlation equations will fail, and provide low correlation coefficients, particularly Eq. (3) corresponding to the red fitted solid line in Fig. 10 (b) with a correlation coefficient of 0.01.

Therefore, when determining a correlation equation between the maximum load and tensile strength, a correlation equation should be determined for brittle materials and ductile materials separately, due to the great difference in mechanical character. However, for ductile materials, although the tensile strength varies greatly, one uniform equation can be observed based on Eq. (2).

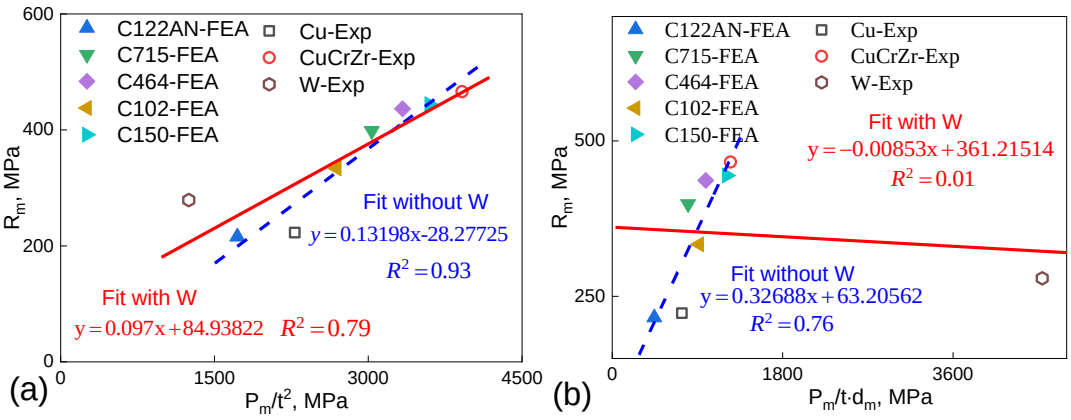

Fig. 10 Correlation between the maximum load and tensile strength: (a) P_m/t^2; (b) $P_m/t{\cdot}d_m$.

3.5.3 Correlation between the displacement at maximum load and fracture elongation

In addition to yield stress and tensile strength, fracture elongation is another important parameter for engineering materials. Rodriguez et al. [42] proposed a correlation equation between the displacement at maximum load of SPT and the fracture elongation of UTT, as follows in Eq. (4):

$$A = \gamma \cdot \frac{d_m}{t} \quad (4)$$

where γ is the correlation parameter, and A is the fracture elongation. Garcia et al. [39] used this equation to predict the fracture elongation of steel by SPT, but found that the predicted fracture elongation was not accurate. Leclerc et al. [43] also found that the above correlation has limited material applicability. Fig. 11 (a) gives the fitting result by Eq. (4) for the materials in this paper. It can be found that whether the data of brittle material W is considered or not, the fitted lines do not agree with the experimental and simulated data. Therefore, Eq. (4) is not suitable for describing the correlation between displacement at maximum load and fracture elongation for the materials studied in this paper.

To improve the applicability of the correlation equation, the intercept is added in Eq. (4) [35, 44] as follows:

$$A = \gamma_1 \cdot \frac{d_m}{t} + \gamma_2 \quad (5)$$

where γ_1, γ_2 are the correlation parameters. NIST [35] used Eq. (5) to correlate the displacement at maximum load and fracture elongation for steels with acceptable correlation coefficients, and Bravo Díez et al. [44] found that Eq. (5) was also suitable for magnesium alloys. Fig. 11 (b) gives the lines fitted via Eq. (5) to the experimental and simulated data. When the brittle material W is not considered, the fitted blue dashed line effectively describes the relationship between the

displacement at maximum load and fracture elongation. However, when the brittle material W is considered, as in the red solid line, the data points deviate significantly from the fitted line, and the correlation coefficient decreases to 0.65.

Therefore, when constructing the correlation equation between the displacement at maximum load and fracture elongation, the correlation equation should be constructed separately for brittle materials and ductile materials. And as shown in Fig. 11 (b), Eq. (5) is effective at correlating the results of SPT and UTT for ductile materials.

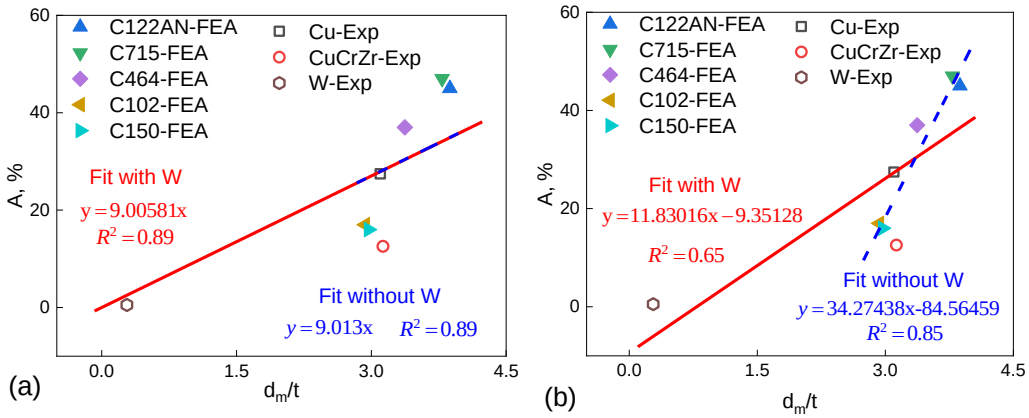

Fig. 11 Correlation between the displacement at maximum load and fracture elongation: (a) Eq. (4); (b) Eq. (5).

4 Conclusion

In this paper, SPT and UTT were carried out on the plasma-facing component materials Cu, CuCrZr and W, and the correlations between SPT and UTT are established with respect to various mechanical properties: load-displacement curve vs. true stress-true strain curve, yield load vs. yield stress, maximum load vs. tensile strength, displacement at maximum load vs. fracture elongation. It is demonstrated that SPT can effectively characterize the variation in mechanical properties and fracture mechanisms exhibited by Cu, CuCrZr and W.

Combining the test results of Cu, CuCrZr and W and the finite element simulation results of five other copper alloys with a wide range of mechanical properties, the quantitative correlation equations of yield load vs. yield stress, maximum load vs. tensile strength, and displacement at maximum load vs. fracture elongation have been established. Although mechanical properties of the ductile materials varied greatly, one unified equation can describe the correlation between SPT and UTT, but the introduction of the brittle material W invalidated the correlation equation. The correlation equations of ductile materials and brittle materials need to be determined separately.

Acknowledgments: The authors are grateful for the supports provided by the National Natural Science Foundation of China, grant number 52075050, Natural Science Foundation of Jiangsu Province, grant number BK20201448, Postgraduate Research & Practice Innovation Program of

Jiangsu Province, grant number, KYCX20_2544, SJCX20_1003. Dr Yiqiang Wang and Dr Mark Richardson would like to acknowledge the RCUK Energy Programme [grant number EP/T012250/1 for time in support of this work.

References

[1] R.E. Stoller, C.H. Henager, N.A. Uckan, Fifteenth international conference on fusion reactor materials, J. Nucl. Mater. 442 (2013) S1. https://doi.org/10.1016/j.jnucmat.2013.08.015.

[2] F. Crescenzi, H. Greuner, S. Roccella, E. Visca, J.H. You, ITER-like divertor target for DEMO: Design study and fabrication test, Fusion. Eng. Des. 124 (2017) 432–436. https://doi.org/10.1016/j.fusengdes.2017.02.014.

[3] Z.X Sun, High heat flux tests and finite element analysis of ITER W/Cu mock-ups(in Chinese), Hefei: University of Science and Technology of China, 2017.

[4] X. Liu, Y. Lian, L. Chen, Z. Cheng, J. Chen, X. Duan, J. Song, Y. Yu, Tungsten joining with copper alloy and its high heat load performance, J. Nucl. Mater. 455 (2014) 382–386. https://doi.org/10.1016/j.jnucmat.2014.07.041.

[5] K. Ezato, S. Suzuki, Y. Seki, H. Yamada, T. Hirayama, K. Yokoyama, F. Escourbiac, T. Hirai, Progress of ITER full tungsten divertor technology qualification in Japan: Manufacturing full-scale plasma-facing unit prototypes, Fusion. Eng. Des. 109–111 (2016) 1256–1260. https://doi.org/10.1016/j.fusengdes.2015.12.049.

[6] E. Visca, E. Cacciotti, A. Komarov, S. Libera, N. Litunovsky, A. Makhankov, A. Mancini, M. Merola, A. Pizzuto, B. Riccardi, S. Roccella, Manufacturing, testing and post-test examination of ITER divertor vertical target W small scale mock-ups, Fusion. Eng. Des. 86 (2011) 1591–1594. https://doi.org/10.1016/j.fusengdes.2011.02.079.

[7] E. Visca, A. Pizzuto, P. Gavila, B. Riccardi, S. Roccella, D. Candura, G.P. Sanguinetti, Technological review of the HRP manufacturing process R&D activity, Fusion. Eng. Des. 88 (2013) 571–576. https://doi.org/10.1016/j.fusengdes.2013.05.031.

[8] Q. Li, S.G. Qin, W.J Wang, P. Qi, S. Roccella, E. Visca, G.H. Liu, G.N. Luo, Manufacturing and testing of W/Cu mono-block small scale mock-up for EAST by HIP and HRP technologies, Fusion. Eng. Des. 88(2013) 1808-1812. https://doi.org/10.1016/j.fusengdes.2013.03.076.

[9] L. Cao, Z. Zhou, D. Yao, EAST Full Tungsten Divertor Design, J. Fusion. Energy. 34 (2015) 1451–1456. https://doi.org/10.1007/s10894-015-9951-2.

[10] Y. Wang, O. Mohamed, K. Dunn, T. Sui, M. Bashir, P. Cooper, A. Lukenskas, G. Wu, M. Gorley, Effects of stress triaxiality and strain rate on the fracture of a CuCrZr alloy, J. Nucl. Mater. 543 (2021) 152546. https://doi.org/10.1016/j.jnucmat.2020.152546.

[11] M.P. Manahan, A.S. Argon, O.K. Harling, The development of a miniaturized disk bend test for the determination of postirradiation mechanical properties, J. Nucl. Mater. 104 (1981) 1545-1550. https://doi.org/10.1016/0022-3115(82)90820-0.

[12] P. Hähner, C. Soyarslan, B. Gülçimen Çakan, S. Bargmann, Determining tensile yield stresses from Small Punch tests: A numerical-based scheme, Mater. Des. 182 (2019) 107974. https://doi.org/10.1016/j.matdes.2019.107974.

[13] E. Altstadt, M. Houska, I. Simonovski, M. Bruchhausen, S. Holmström, R. Lacalle, On the estimation of ultimate tensile stress from small punch testing, Int. J. Mech. Sci. 136 (2018) 85–93. https://doi.org/10.1016/j.ijmecsci.2017.12.016.

[14] W. Wang, J. Zhong, X. Zhang, T. Jiang, K. Guan, Study of estimation of ductile-brittle transition temperature using U-notched small punch test specimens, Theor. Appl. Fract. Mech. 108 (2020) 102627. https://doi.org/10.1016/j.tafmec.2020.102627.

[15] R. Hurst, Y. Li, K. Turba, Determination of fracture toughness from the small punch test using circular notched specimens, Theor. Appl. Fract. Mech. 103 (2019) 102238. https://doi.org/10.1016/j.tafmec.2019.102238.

[16] L.Y. Wang, Z.J. Zhou, C.P. Li, G.F. Chen, G.P. Zhang, Comparative investigation of small punch creep resistance of Inconel 718 fabricated by selective laser melting, Mater. Sci. Eng., A. 745 (2019) 31–38. https://doi.org/10.1016/j.msea.2018.12.083.

[17] J. Peng, V.D. Vijayanand, D. Knowles, C. Truman, M. Mostafavi, The sensitivity ranking of ductile material mechanical properties, geometrical factors, friction coefficients and damage parameters for small punch test, Int. J. Pressure Vessels Piping. 193 (2021) 104468. https://doi.org/10.1016/j.ijpvp.2021.104468.

[18] V.D. Vijayanand, M. Mokhtarishirazabad, J. Peng, Y. Wang, M. Gorley, D.M. Knowles, M. Mostafavi, A novel methodology for estimating tensile properties in a small punch test employing in-situ DIC based deflection mapping, J. Nucl. Mater. 538 (2020) 152260. https://doi.org/10.1016/j.jnucmat.2020.152260.

[19] S. Arunkumar, Overview of Small Punch Test, Met. Mater. Int. 26 (2020) 719–738. https://doi.org/10.1007/s12540-019-00454-5.

[20] P. Kumar, B.K. Dutta, J. Chattopadhyay, R.S. Shriwastaw, Numerical evaluation of J-R curve using small punch test data, Theor. Appl. Fract. Mech. 86 (2016) 292–300. http://doi.org/10.1016/j.tafmec.2016.08.003.

[21] I. Simonovski, D. Baraldi, S. Holmström, E. Altstadt, R. Delville, M. Bruchhausen, Determining the ultimate tensile strength of fuel cladding tubes by small punch testing, J. Nucl. Mater. 509 (2018) 620–630. https://doi.org/10.1016/j.jnucmat.2018.07.041.

[22] I. Simonovski, S. Holmström, D. Baraldi, R. Delville, Investigation of cracking in small punch test for semi-brittle materials, Theor. Appl. Fract. Mech. 108 (2020) 102646. https://doi.org/10.1016/j.tafmec.2020.102646.

[23] X. Zhang, C. Zhang, Z. Ding, Y. Chen, L. Zhang, Quantification of the constitutive relationship of high-energy heavy-ion irradiated SS316L using the small punch test, J. Nucl. Mater. 531 (2020) 152014. https://doi.org/10.1016/j.jnucmat.2020.152014.

[24] C.F. Yao, Y. Dai, DBTT shift of Optifer-IX, DBTT shift of Optifer-IX, Eurofer 97 and MA956 steels after irradiation evaluated with small punch tests, J. Nucl. Mater. 544 (2021) 152725. https://doi.org/10.1016/j.jnucmat.2020.152725.

[25] V.D. Vijayanand, M. Mokhtarishirazabad, Y. Wang, M. Gorley, D.M. Knowles, M. Mostafavi, Estimating damage parameters of a CuCrZr alloy subjected to two varying heat treatments using small punch test, J. Nucl. Mater. 557 (2021) 153263. https://doi.org/10.1016/j.jnucmat.2021.153263.

[26] M. Richardson, M. Gorley, Y. Wang, D. Andres, H. Dawson, Small punch creep investigation of Eurofer97 and 14Cr oxide dispersion strengthened steel, Nucl. Mater. Energy. 29 (2021)101067. https://doi.org/10.1016/j.nme.2021.101067

[27] GB/T 29459. 2-2012, Small punch test methods of metallic materials for in-service pressure equipments. Part 2: Method of test for tensile properties at room temperature.

[28] GB/T 228. 1-2010, Metallic materials. Tensile testing. Part 1: Method of test at room

temperature.
[29] X. Mao, H. Takahashi, Development of a further-miniaturized specimen of 3 mm diameter for tem disk (ø 3 mm) small punch tests, J. Nucl. Mater. 150 (1987) 42–52. https://doi.org/10.1016/0022-3115(87)90092-4.
[30] M.F. Moreno, G. Bertolino, A. Yawny, The significance of specimen displacement definition on the mechanical properties derived from Small Punch Test, Mater. Des. 95 (2016) 623–631. https://doi.org/10.1016/j.matdes.2016.01.148.
[31] CEN Workshop Agreement, CWA 15627:2006 E, Small Punch Test Method for Metallic Materials, CEN, Brussels, 2006.
[32] M.A. Contreras, C. Rodríguez, F.J. Belzunce, C. Betegón, Use of the small punch test to determine the ductile-to-brittle transition temperature of structural steels, Fatigue Fract. Eng. Mater. Struct. 31 (2008) 727–737. https://doi.org/10.1111/j.1460-2695.2008.01259.x.
[33] S.R. Ghodke, B.K. Dutta, P. v. Durgaprasad, Analytical development and experimental verification of empirical correlations to determine mechanical properties of copper alloys using small punch test data, Fusion Eng. Des. 159 (2020) 111786. https://doi.org/10.1016/j.fusengdes.2020.111786.
[34] Publications List/Properties/Standards/144/8R/Low temperature properties of copper and copper alloys, https://www.copper.org/publications/pub_list/properties_standards.html.
[35] E. Lucon, J. Benzing, N. Hrabe, Development and validation of small punch testing at NIST, Gaithersburg, MD, 2020. https://doi.org/10.6028/NIST.IR.8303.
[36] M. Song, X. Li, Y. Cao, Y. Zhen, J. Zhong, K. Guan, Determination of elastoplastic properties of in-service pipeline steel based on backpropagation neural network and small punch test, Int. J. Pressure Vessels Piping. 190 (2021) 104316. https://doi.org/10.1016/j.ijpvp.2021.104316.
[37] M.F. Moreno, M. Balog, P. Krizik, Mechanical characterization of PM aluminum composites by small punch test, Rev. Mater. 23 (2018). https://doi.org/10.1590/S1517-707620180002.0357.
[38] J. Torres, A.P. Gordon, Mechanics of the small punch test: a review and qualification of additive manufacturing materials, J. Mater. Sci. 56 (2021) 10707–10744. https://doi.org/10.1007/s10853-021-05929-8.
[39] T.E. García, C. Rodríguez, F.J. Belzunce, C. Suárez, Estimation of the mechanical properties of metallic materials by means of the small punch test, J. Alloys Compd. 582 (2014) 708–717. https://doi.org/10.1016/j.jallcom.2013.08.009.
[40] K. Kumar, K. Madhusoodanan, R.N. Singh, Miniature test techniques for life management of operating equipment, Nucl. Eng. Des. 323 (2017) 345–358. https://doi.org/10.1016/j.nucengdes.2017.03.007.
[41] J.C. Chica, P.M.B. Díez, M.P. Calzada, A New Prediction Method for the Ultimate Tensile Strength of Steel Alloys with Small Punch Test, Materials. 11 (2018) 1491. https://doi.org/10.3390/ma11091491.
[42] C. Rodríguez, J. García Cabezas, E. Cárdenas, F.J. Belzunce, C. Betegón, Mechanical properties characterization of heat-affected zone using the small punch test, Weld. J. 88 (2009) 188–192.
[43] N. Leclerc, A. Khosravani, S. Hashemi, D.B. Miracle, S.R. Kalidindi, Correlation of Measured Load-Displacement Curves in Small Punch Tests with Tensile Stress-Strain Curves, Acta Mater. 204 (2021) 116501. https://doi.org/10.1016/j.actamat.2020.116501.

[44] P.M. Bravo Díez, M. Preciado Calzada, D. Cárdenas Gonzalo, J. Calaf Chica, Change of mechanical properties of AM60B alloy with heat treatments and its correlation with small punch tests, Theor. Appl. Fract. Mech. 86 (2016) 101–108. https://doi.org/10.1016/j.tafmec.2016.09.014.